

Electronic Structure of Four-Coordinate C_{3v} Nickel(II) Scorpionate Complexes: Investigation by High-Frequency and -Field Electron Paramagnetic Resonance and Electronic Absorption Spectroscopies

Patrick J. Desrochers,^{*,†} Joshua Telser,[‡] S. A. Zvyagin,[§] Andrew Ozarowski,^{||} J. Krzystek,^{||} and David A. Vovic[⊥]

Department of Chemistry, University of Central Arkansas, Conway, Arkansas 72035, Department of Biological, Chemical and Physical Sciences, Roosevelt University, Chicago, Illinois 60605, Dresden High Magnetic Field Laboratory (HLD), Forschungszentrum Rossendorf, D-01328 Dresden, Germany, National High Magnetic Field Laboratory, Florida State University, Tallahassee, Florida 32310, and Department of Chemistry and Biochemistry, University of Arkansas, Fayetteville, Arkansas 72701

Received May 16, 2006

A series of complexes of formula Tp^*NiX , where Tp^{*-} = hydrotris(3,5-dimethylpyrazole)borate and $X = Cl, Br, I$, has been characterized by electronic absorption spectroscopy in the visible and near-infrared (NIR) region and by high-frequency and -field electron paramagnetic resonance (HF-EPR) spectroscopy. The crystal structure of Tp^*NiCl has been previously reported; that for Tp^*NiBr is given here: space group = $Pmc2_1$, $a = 13.209(2)$ Å, $b = 8.082(2)$ Å, $c = 17.639(4)$ Å, $\alpha = \beta = \gamma = 90^\circ$, $Z = 4$. Tp^*NiX contains a four-coordinate nickel(II) ion ($3d^8$) with approximate C_{3v} point group symmetry about the metal and a resulting $S = 1$ high-spin ground state. As a consequence of sizable zero-field splitting (zfs), Tp^*NiX complexes are “EPR silent” with use of conventional EPR; however, HF-EPR allows observation of multiple transitions. Analysis of the resonance field versus the frequency dependence of these transitions allows extraction of the full set of spin Hamiltonian parameters. The axial zfs parameter for Tp^*NiX displays pronounced halogen contributions down the series: $D = +3.93(2), -11.43(3), -22.81(1)$ cm^{-1} , for $X = Cl, Br, I$, respectively. The magnitude and change in sign of D observed for Tp^*NiX reflects the increasing bromine and iodine spin-orbit contributions facilitated by strong covalent interactions with nickel(II). These spin Hamiltonian parameters are combined with estimates of 3d energy levels based on the visible-NIR spectra to yield ligand-field parameters for these complexes following the angular overlap model (AOM). This description of electronic structure and bonding in a pseudotetrahedral nickel(II) complex can enhance the understanding of similar sites in metalloproteins, both native nickel enzymes and nickel-substituted zinc enzymes.

Introduction

A paramagnetic high-spin ground state (HS) with $S = 1$ in nickel(II) ($3d^8$) is common for six-coordinate octahedral, five-coordinate trigonal bipyramidal/square pyramidal, and four-coordinate tetrahedral geometries. Diamagnetic nickel(II) ($S = 0$) is the other magnetic extreme for this ion

and is invariably associated with square planar coordination. Investigation of the electronic structural basis of HS nickel(II) chemistry by electron paramagnetic resonance (EPR) is often fruitless because of the large zero-field splittings (zfs), which impede conventional X-band (~ 9 GHz) and Q-band (35 GHz) EPR measurements. In such cases, HS nickel(II) has often been termed an “EPR silent” ion.

The novel technique of high-frequency and -field EPR (HF-EPR, defined here as frequencies above ~ 95 GHz and magnetic fields above ~ 3 T) overcomes the above difficulty.

HF-EPR has been recently applied to HS nickel(II) in a range of complexes.^{1–9} These studies include six-coordinate

* To whom correspondence should be addressed. E-mail: patrickd@uca.edu.

† University of Central Arkansas.

‡ Roosevelt University.

§ Dresden High Magnetic Field Laboratory (HLD).

|| Florida State University.

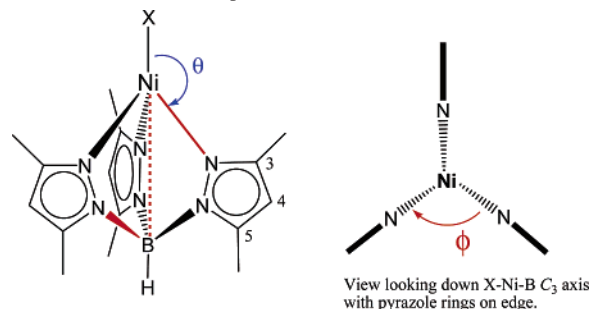
⊥ University of Arkansas.

pseudo-octahedral nickel(II) with various nitrogen and oxygen-donor sets^{3–7} and four-coordinate pseudotetrahedral nickel(II) with phosphorus and halide donor sets.^{1,2} HFEPR is therefore emerging as an effective tool for probing the magnetic and electronic characteristics of HS nickel(II).

The extension of the application of HFEPR to a wider variety of HS nickel(II) complexes is relevant to the eventual application of this technique to biological systems. For example, high-spin four/five-coordinate nickel(II) centers are postulated to represent the EPR silent states of nickel hydrogenase enzymes^{10,11} and the reduced states of the C-cluster in bacterial carbon monoxide dehydrogenases.¹² Furthermore, the zinc(II) centers in metalloproteins have been substituted with nickel(II) to provide HS forms suitable for study by other spectroscopic techniques,^{13,14} and could prove suitable for study by HFEPR as well.

In this work, we consider a ligand appropriate for the generation of HS nickel(II) complexes with biologically relevant donor atoms. Tris(pyrazolyl)borates (Tp^{Y-} “scorpionates”),^{15,16} where Y represents variable substitution at the 3-, 4-, or 5-pyrazole ring positions (Scheme 1), are widely regarded as effective models of nitrogen-donor histidine ligands. Four-coordinate Tp^YMX complexes are typically high spin (M = Mn, Fe, Co, Ni, Cu; X = halides and pseudohalides, such as NCS⁻, NCO⁻, and N₃⁻). Over the last twenty years, the general method of preparing pseudotetrahedral Tp^YNiX complexes involved the use of Tp^{Y-} derivatives with sterically encumbered 3-position (Y) substituents. Accord-

Scheme 1. Structure of Tp^YNiX^a



^a Pyrazole ring 3,4,5-substituents can be varied to give a range of Tp^{Y-} ligands. Bond angles used in the AOM are indicated. The X–Ni–N angles represent θ (in blue). The N–B–Ni–N vectors define the torsional angles that are used to determine ϕ (in red).

ingly, complexes with isopropyl-, *tert*-butyl-, neopentyl-, *p*-tolyl-, and phenyl-substituted pyrazoles have all been used to prepare a variety of formally C_{3v} Tp^YNiX complexes, and some have been structurally characterized.^{17–20}

The HS Tp^YNiX complexes of the present study, shown in Scheme 1 (Tp^{Y-} = hydrotris(3,5-dimethylpyrazole)borate), represent a complete series of nickel halides with formal C_{3v} symmetry. No similar series has been reported for any other [Tp^YNi]⁺ system. These Tp^YNiX complexes are remarkably stable despite the smaller methyl substituents of Tp^{Y-} versus the aforementioned more sterically demanding groups. Electronic factors must therefore also play a role in the resistance of Tp^YNiX to form thermodynamic products such as (Tp^{Y-})₂Ni.²¹

The present work summarizes HFEPR and visible/near-infrared (NIR) electronic absorption spectral measurements for the series of Tp^YNiX complexes (X = Cl, Br, I). The crystal structure of Tp^YNiBr is also reported, adding to earlier results for Tp^YNiCl.²² Ligand-field calculations based on the angular overlap model (AOM)^{23,24} are used to correlate these independent spectral measurements and extract σ - and π -bonding information for the nitrogen- and halogen-donor atoms in these complexes. The following results for these formally C_{3v} HS nickel(II) centers complement more limited measurements previously reported for C_{2v} nickel(II) systems¹ and further demonstrate both the utility of HFEPR for the characterization of HS nickel(II) and the importance of ligand effects on electronic structure.

Experimental Section

Synthesis and Purification of Tp^YNiX Complexes. These complexes were prepared via dehalogenation reactions of Tp^YNiBH₄ with appropriate alkyl halides: CCl₄, CBr₄, and CHI₃. Solid alkyl

- (1) Krzystek, J.; Park, J.-H.; Meisel, M. W.; Hitchman, M. A.; Strateimer, H.; Brunel, L.-C.; Telsler, J. *Inorg. Chem.* **2002**, *41*, 4478–4487.
- (2) Vongtragool, S.; Gorshunov, B.; Dressel, M.; Krzystek, J.; Eichhorn, D. M.; Telsler, J. *Inorg. Chem.* **2003**, *42*, 1788–1790.
- (3) Pardi, L. A.; Hassan, A. K.; Hulsbergen, F. B.; Reedijk, J.; Spek, A. L.; Brunel, L.-C. *Inorg. Chem.* **2000**, *39*, 159–164.
- (4) Collison, D.; Helliwell, M.; Jones, V. M.; Mabbs, F. E.; McInnes, A. J. L.; Riedi, P. C.; Smith, G. M.; Pritchard, R. G.; Cross, W. I. *J. Chem. Soc., Faraday Trans.* **1998**, *94*, 3019–3025.
- (5) Mrozinski, J.; Skorupa, A.; Pochaba, A.; Dromzee, Y.; Verdager, M.; Goovaerts, E.; Varcammen, H.; Korybut-Daszkiwicz, B. *J. Mol. Struct.* **2001**, *559*, 107–118.
- (6) Yang, E.-C.; Kirman, C.; Lawrence, J.; Zakharov, L. N.; Rheingold, A. L.; Hill, S.; Hendrickson, D. N. *Inorg. Chem.* **2005**, *44*, 3827–3836.
- (7) Rogez, G.; Rebilly, J.-N.; Barra, A.-L.; Sorace, L.; Blondin, G.; Kirchner, N.; Duran, M.; van Slageren, J.; Parsons, S.; Ricard, L.; Marvilliers, A.; Mallah, T. *Angew. Chem., Int. Ed.* **2005**, *44*, 1876–1879.
- (8) Orendác, M.; Zvyagin, S.; Orendácová, A.; Sieling, M.; Lüthi, B.; Feher, A.; Meisel, M. W. *Phys. Rev. B* **1999**, *60*, 4170–4175.
- (9) Orendác, M.; Cizmár, E.; Orendácová, A.; Cernák, J.; Feher, A.; Meisel, M. W.; Abboud, K. A.; Zvyagin, S.; Sieling, M.; Rieth, T.; Lüthi, B. *Phys. Rev. B* **2000**, *61*, 3223–3226.
- (10) Stadler, C.; de Lacey, A. L.; Montet, Y.; Volbeda, A.; Fontecilla-Camps, J. C.; Conesa, J. C.; Fernandez, V. M. *Inorg. Chem.* **2002**, *41*, 4424–4434.
- (11) Wang, H.; Ralston, C. Y.; Patil, D. S.; Jones, R. M.; Gu, W.; Verhagen, M.; Adams, M.; Ge, P.; Riordan, C.; Marganian, C. A.; Mascharak, P.; Kovacs, J.; Miller, C. G.; Collins, T. J.; Brooker, S.; Croucher, P. D.; Wang, K.; Stiefel, E. I.; Cramer, S. P. *J. Am. Chem. Soc.* **2000**, *122*, 10544–10552.
- (12) Ralston, C. Y.; Wang, H.; Ragsdale, S. W.; Kumar, M.; Spangler, N. J.; Ludden, P. W.; Gu, W.; Jones, R. M.; Patil, D. S.; Cramer, S. P. *J. Am. Chem. Soc.* **2000**, *122*, 10553–10560.
- (13) Bal, W.; Schwerdtle, T.; Hartwig, A. *Chem. Res. Toxicol.* **2003**, *16*, 242–248.
- (14) Xu, Y.; Wilcox, D. E. *J. Am. Chem. Soc.* **1998**, *120*, 7375–7376.
- (15) Trofimenko, S. *Scorpionates: The Coordination Chemistry of Polypyrazolylborate Ligands*; Imperial College Press: London, U.K., 1999.
- (16) Trofimenko, S. *Polyhedron* **2004**, *23*, 197–203.

- (17) Trofimenko, S.; Calabrese, J. C.; Kochi, J. K.; Wolowiec, S.; Hulsbergen, F. B.; Reedijk, J. *Inorg. Chem.* **1992**, *31*, 3943–3950.
- (18) Uehara, K.; Hikichi, S.; Akita, M. *J. Chem. Soc., Dalton Trans.* **2002**, 3529–3538.
- (19) Shirasawa, N.; Nguyen, T. T.; Hikichi, S.; Moro-oka, Y.; Akita, M. *Organometallics* **2001**, *20*, 3582–3598.
- (20) Guo, S.; Ding, E.; Yin, Y.; Yu, K. *Polyhedron* **1998**, *17*, 3841–3849.
- (21) Trofimenko, S. *J. Am. Chem. Soc.* **1967**, *89*, 6288–6294.
- (22) Desrochers, P. J.; LeLievre, S.; Johnson, R. J.; Lamb, B. T.; Phelps, A. L.; Cordes, A. W.; Gu, W.; Cramer, S. P. *Inorg. Chem.* **2003**, *42*, 7945–7950.
- (23) Figgis, B. N.; Hitchman, M. A. *Ligand Field Theory and its Applications*; Wiley-VCH: New York, 2000.
- (24) Schäffer, C. E. *Struct. Bonding* **1968**, *5*, 68–95.

halides were dissolved in dichloromethane and reacted with a dichloromethane solution of Tp^*NiBH_4 . Carbon tetrachloride was reacted as a neat liquid. Details of the synthesis and purification of Tp^*NiBH_4 and all Tp^*NiX are described elsewhere.²² It should be noted that these same three Tp^*NiX complexes can also be synthesized by the two-phase reaction of $\text{Tp}^*\text{Ni}(\text{acac})$ in dichloromethane mixed with the appropriate aqueous HX solution.²⁵

Electronic Absorption Spectroscopy. UV-vis spectra were recorded for samples of the respective Tp^*NiX complexes dissolved in both dichloromethane and carbon tetrachloride. UV-vis spectra (50 000–9000 cm^{-1}) were recorded at ambient temperature in CH_2Cl_2 using a Varian Cary 50 spectrophotometer and 1 cm quartz cuvettes. A Jasco 570 UV-vis-NIR spectrophotometer with samples in Suprasil cuvettes was used to record electronic absorption spectra from 25 000 to 4000 cm^{-1} at ambient temperature. Only carbon tetrachloride was used for NIR spectra because the C–H stretch overtones greatly complicate the NIR region in CH_2Cl_2 solvent.

HFEPR Spectroscopy. HFEPR spectra were recorded using primarily the Millimeter and Submillimeter Wave Facility at NHMFL,²⁶ with some experiments performed at the EMR Facility.²⁷ The former experimental setup employs tunable frequencies in the 150–700 GHz range and the resistive “Keck” magnet, enabling 0–25 T field sweeps. Detection was provided with an InSb hot-electron bolometer (QMC Ltd., Cardiff, U.K.). Modulation for detection purposes was provided alternatively by chopping the subterahertz wave beam (“optical modulation”) or by modulating the magnetic field. A Stanford Research Systems SR830 lock-in amplifier converted the modulated signal to DC voltage.

Typically, 30–50 mg of solid sample was used for HFEPR. In previous HFEPR studies of magnetically nondiluted solid nickel(II) samples, magnetic field-induced torquing of microcrystallites occurred.²⁸ In this work, such effects were observed for Tp^*NiI but not for the other two complexes. Tp^*NiBr gave powder-patterned HFEPR spectra; however, Tp^*NiCl produced spectra that were neither field-oriented nor powder-patterned. The tunable-frequency methodology employed here nevertheless allowed us to identify particular turning points within the nonideal powder patterns for Tp^*NiCl and accurately determine spin Hamiltonian parameters. The sign of D could not be directly determined from this type of experiment (see below). Frozen solutions would of course provide ideal powder-pattern spectra, but Tp^*NiCl has very limited solubility in noncoordinating solvents (such as those used for electronic absorption studies). Thus, frozen solution studies of the four-coordinate form of the molecule, as found in the solid state and in noncoordinating solvents, were not possible.

EPR Analysis. The magnetic properties of an ion with $S = 1$ can be described by the standard spin Hamiltonian composed of Zeeman and zfs terms²⁹

$$\mathcal{H} = \beta B g S + D(S_z^2 - S(S+1)/3) + E(S_x^2 - S_y^2) \quad (1)$$

The canonical resonance field versus the frequency dependencies were fitted using a nonlinear least-squares procedure based on the

- (25) Cleland, W. E. University of Mississippi, Oxford, MS. Private communication (acac = acetylacetonate).
 (26) Zvyagin, S. A.; Krzystek, J.; van Loosdrecht, P. H. M.; Dhalenne, G.; Revcolevschi, A. *Phys. B* **2004**, *346–347*, 1–5.
 (27) Hassan, A. K.; Pardi, L. A.; Krzystek, J.; Sienkiewicz, A.; Goy, P.; Rohrer, M.; Brunel, L.-C. *J. Magn. Reson.* **2000**, *142*, 300–312.
 (28) Krzystek, J.; Telsler, J.; Pardi, L. A.; Goldberg, D. P.; Hoffman, B. M.; Brunel, L.-C. *Inorg. Chem.* **1999**, *38*, 6121–6129.
 (29) Abragam, A.; Bleaney, B. *Electron Paramagnetic Resonance of Transition Ions*; Dover Publications: New York, 1986.

well-known formulas resulting from the exact solution of the secular equation for the triplet state.³⁰ Further details of the tunable-frequency EPR methodology are given elsewhere.³¹

AOM Analysis. Analysis of the electronic structure of Ni(II) in Tp^*NiX complexes was performed with use of the angular overlap model (AOM).²³ Two computer programs were employed, Ligfield, written by J. Bendix (Ørsted Institute, Copenhagen, Denmark)³² and a locally written program, DDN (available from J.T.). Both programs use the complete d^8 (equivalent to d^2) weak-field basis set including interelectronic repulsion (Racah parameters, B and C), spin-orbit coupling (SOC constant, ζ), and AOM ligand-field bonding parameters (ϵ_σ and ϵ_π) and gave identical results when directly compared. DDN allows the use of a nonlinear least-squares fitting subroutine (DSTEPIT, from QCPE, Bloomington, IN) to match observed electronic transition energies to those calculated by user-defined variable parameters such as B , ϵ_σ , etc. The general AOM procedure involved an initial fit of spin-allowed optical transitions (as recorded in CCl_4 solution; the more inert of the two solvents employed) with variation of Racah B and AOM bonding parameters and with $\zeta \equiv 0$ (and C very large). To make the fitting tractable, the bonding parameters for the three pyrazole N-donors were held identical (i.e., imposed C_3 bonding symmetry). From this initial fit, ζ was systematically varied (along with $C \equiv 4.7B$; the use of the ratios $C/B = 4.3$ and 4.9 affected the value of D calculated for Tp^*NiCl by only $\sim 1\%$) until a reasonable match was obtained for $|D|$ in relation to experimental values. The resulting electronic transitions were then checked to ensure that they were still in agreement with the experiment. DDN also allows inclusion of an external magnetic field to be applied along the molecular axes (defined by the AOM) to give the Zeeman splitting of energy levels from which the g values can be calculated, as described previously.³³

X-ray Crystallography of Tp^*NiBr . A pink block crystal of Tp^*NiBr measuring $0.35 \times 0.35 \times 0.30$ mm was grown by slow evaporation of a dichloromethane solution of the compound. A total of 4732 unique reflections (3771 with $I > 2\sigma$) were collected at ambient temperature using a Rigaku-AFC8-Mercury CCD diffractometer. The structure was solved by direct methods and expanded using Fourier techniques.³⁴ The non-hydrogen atoms were refined anisotropically. Hydrogen atoms were included as riding atoms but not refined. The standard deviation of an observation of unit weight was calculated. All calculations were performed using the software CrystalClear³⁵ and CrystalStructure (version 1.3.6) from Rigaku³⁶ and CRYSTALS, issue 10, by Watkin et al.³⁷ except for refinement, which was performed using SHELX-97.

- (30) Kottis, P.; Lefebvre, R. *J. Chem. Phys.* **1964**, *41*, 379–393.
 (31) Krzystek, J.; Zvyagin, S. A.; Ozarowski, A.; Trofimenko, S.; Telsler, J. *J. Magn. Reson.* **2006**, *178*, 174–183.
 (32) Bendix, J.; Brorson, M.; Schäffer, C. E. *Inorg. Chem.* **1993**, *32*, 2838–2849.
 (33) Krzystek, J.; Fiedler, A. T.; Sokol, J. J.; Ozarowski, A.; Zvyagin, S. A.; Brunold, T. C.; Long, J. R.; Brunel, L.-C.; Telsler, J. *Inorg. Chem.* **2004**, *43*, 5645–5658.
 (34) Beurskens, P. T.; Admiraal, G.; Beurskens, G.; Bosman, W. P.; de Gelder, R.; Israel, R.; Smits, M. M. *The DIRDIF-99 program system*; Technical Report of the Crystallography Laboratory; University of Nijmegen: Nijmegen, The Netherlands, 1999.
 (35) *CrystalClear Software User's Guide*; Molecular Structure Corporation: The Woodlands, TX, 1999.
 (36) *Rigaku and Rigaku/MS*, 3.6.0 ed.; Molecular Structure Corporation: The Woodlands, TX, 2000–2004.
 (37) Watkin, D. J.; Prout, C. K.; Carruthers, J. R.; Betteridge, P. W. *CRYSTALS*, issue 10; Chemical Crystallography Laboratory, University of Oxford: Oxford, U.K., 1996.

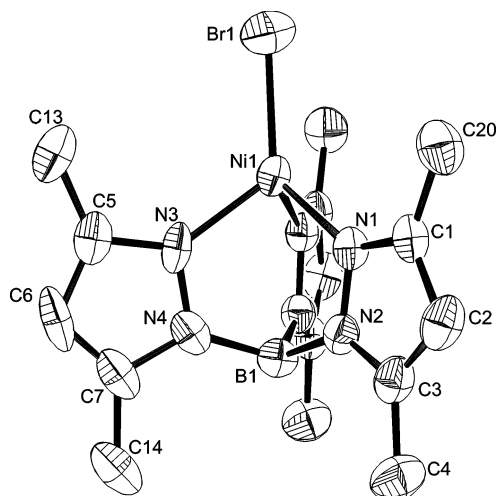


Figure 1. ORTEP plot of molecule 1, one of two slightly different Tp^*NiBr molecules in the asymmetric unit (50% probability ellipsoids, hydrogen atoms omitted). The unlabeled pyrazole ring at back is the symmetry equivalent of the N1,N2 ring related by a mirror plane containing the N3,N4 pyrazole ring. For molecules 1 and 2, respectively, the Ni–Br distances (Å) are 2.293(1) and 2.289(1), the Ni–N distances (Å) are Ni1–N1 = 1.968(4), Ni1–N3 = 1.957(6), Ni2–N5 = 1.987(5), and Ni2–N8 = 1.966(4), and the Br–Ni–N angles (deg) are Br1–Ni1–N3 = 122.77(19), Br1–Ni1–N1 = 124.00(12), Br2–Ni2–N5 = 120.81(17), and Br2–Ni2–N8 = 124.80(13). See Supporting Information (CIF file and Table S1) for a complete listing of distances and angles for both molecules.

Results

Crystal and Molecular Structure of Tp^*NiBr . Tp^*NiBr crystallizes in an orthorhombic space group with unit cell dimensions only about 2% larger than those observed for Tp^*NiCl .²² Just as for Tp^*NiCl ,²² two slightly different Tp^*NiBr molecules crystallized in the asymmetric unit (Figure 1). These two molecules differ by ± 0.004 Å in Ni–Br and 0.03 Å in Ni–N distances, and by $\pm 4^\circ$ in N–Ni–Br and 2° in N–Ni–N angles. The crystallographic results are summarized in Table 1 (and Tables S1 and S2). The average nickel–nitrogen bond length in Tp^*NiBr , 1.970(17) Å, is typical of four-coordinate Tp^*Ni –nickel distances.^{17–20,22} The average nickel–bromine distance, 2.291(2) Å, is 0.12 Å longer than the corresponding nickel–chlorine distance, similar to the 0.14 Å difference observed for $\text{Tp}^{\text{bu}}\text{ZnCl}$ and $\text{Tp}^{\text{bu}}\text{ZnBr}$ ³⁸ and consistent with the difference in bromine and chlorine covalent radii (0.15 Å).³⁹ Both molecules of the asymmetric unit have geometries that deviate from perfect C_{3v} symmetry, in part, as a result of differences in the Br–Ni–N and N–Ni–N angles about the idealized 3-fold axis defined by Br–Ni–B. Differences of 1–4° in these angles within the same molecule is not unique to Tp^*NiX , but rather it is a general feature observed in the majority of structurally characterized Tp^*R –metal–halide complexes; one that likely results from packing influences of the Tp^*R ligands. A rare example of a Tp^*R –metal–halide complex that does have a C_3 axis is $\text{Tp}^{\text{ph}_2}\text{NiCl}$.²⁰ However, it is quite likely that in solution, $\text{Tp}^*\text{R}^{\text{M}}\text{X}$ complexes generally exhibit 3-fold symmetry (see below).

Electronic Absorption Spectroscopy of Tp^*NiX . Qualitatively similar electronic absorption spectra were recorded

Table 1. Crystal, Collection, and Refinement Parameters for Tp^*NiBr

empirical formula	$\text{C}_{15}\text{H}_{20}\text{BBrN}_6\text{Ni}$
fw	433.80
cryst size	$0.35 \times 0.35 \times 0.30$ mm
temp	298(2) K
wavelength	0.71070 Å
space group	orthorhombic, $Pmc2_1$
cell dimensions	$a = 13.209(2)$ Å $b = 8.0823(16)$ Å $c = 17.639(4)$ Å $\alpha = \beta = \gamma = 90^\circ$
vol	$1883.1(6)$ Å ³
Z, density (calcd)	4, 1.53 g/cm ³
abs coeff	3.161 mm ⁻¹
$F(000)$	880
2θ range	5 – 56°
limiting indices	$-17 \leq h \leq 14$, $-8 \leq k \leq 10$, $-23 \leq l \leq 23$
unique reflns	4732
reflns refined	3771 [$I > 2\sigma(I)$]
params	258
GOF	1.062
R, R_w^a (all reflns)	0.0683, 0.1370
R, R_w^a ($I > 2\sigma(I)$)	0.0532, 0.1268
final max/min peak	0.796, -0.591 e/Å ³

$$^a R = \frac{\sum [(|F_o| - |F_c|)] / \sum |F_o|}{\sum |F_o|}, R_w = \frac{\{\sum [w(F_o^2 - F_c^2)^2] / \sum [w(F_o^2)^2]\}^{1/2}}{w = 1 / [\sigma^2(F_o^2) + (0.0622P)^2 + 0.4079P]}, \text{ where } P = (F_o^2 + 2F_c^2) / 3.$$

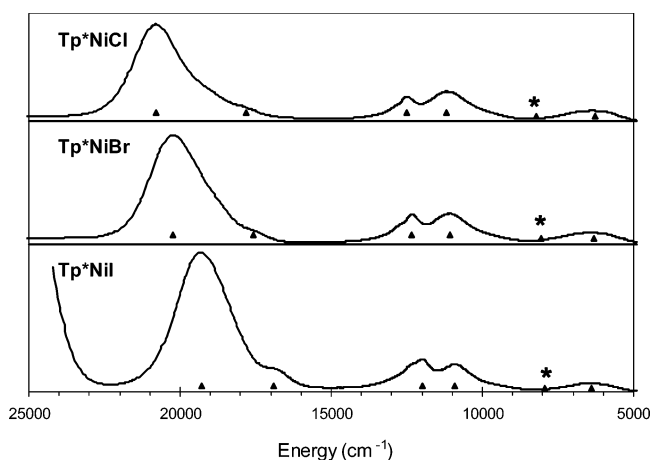


Figure 2. Vis–NIR electronic absorption spectra of Tp^*NiX ($X = \text{Cl}, \text{Br}, \text{I}$) dissolved in CCl_4 . Absorbance scales are arbitrary for the purpose of comparison (see Table 2 for molar absorptivities). Black triangles are centered at calculated spin-allowed (triplet) transition energies for idealized C_{3v} symmetry (see text and Table 2). Asterisks mark the 3A_2 ($^3T_1, F$) \rightarrow 3A_1 ($^3T_2, F$) transition, which is forbidden in C_{3v} symmetry.

for all three complexes, and these spectra are consistent with the general ligand field-transition energy trend for the halide series. Vis–NIR spectra are shown in Figure 2, and the complete UV–vis–NIR range is shown in Figure S1. The band energies and molar absorptivities are summarized in Table 2. Strong bands are seen in the UV region, which are red-shifted and more intense from Cl to Br to I and, thus, are most likely LMCT bands (qualitatively $\text{Ni}^{\text{I}}\text{–X}^*$). This assignment is also supported by the redox behavior of [(triphos)Ni^{II}X]⁺ ($X = \text{Cl}, \text{Br}, \text{I}$; triphos = 1,1,1-tris-(diphenylphosphinomethyl)ethane) cations that possess pseudotetrahedral P_3NiX coordination spheres.⁴⁰ All three

(38) Yoon, K.; Parkin, G. *J. Am. Chem. Soc.* **1991**, *113*, 8414–8418.

(39) Shannon, R. D. *Acta Crystallogr.* **1976**, *A32*, 751–767.

(40) Zanello, P.; Cinquantini, A.; Ghilardi, C. A.; Midollini, S.; Moneti, S.; Orlandini, A.; Bencini, A. *J. Chem. Soc., Dalton Trans.* **1990**, 3761–3766.

Table 2. Solution-Phase Electronic Transitions (cm^{-1}), Molar Absorptivities ($\text{M}^{-1} \text{cm}^{-1}$), and Theoretical Transitions and Assignments Predicted by AOM Analysis for Tp^*NiX

		assignment ^a							
		CT	CT	${}^3\text{A}_2$ (${}^3\text{A}_2, \text{F}$)	${}^3\text{E}$ (${}^3\text{T}_1, \text{P}$)	${}^3\text{A}_2$ (${}^3\text{T}_1, \text{P}$)	${}^3\text{E}$ (${}^3\text{T}_2, \text{F}$)	${}^3\text{A}_1$ (${}^3\text{T}_2, \text{F}$)	${}^3\text{E}$ (${}^3\text{T}_1, \text{F}$)
Tp^*NiCl	in CH_2Cl_2	40 000 (6000)	30 960 (840)	20 790 (500)	17 850 (70, sh)	12 590 (150)	11 330 (170)		
	in CCl_4		31 300 (680)	20 800 (470)	17 800 (80, sh)	12 520 (125)	11 200 (150)	absent ^b	6290 (55)
	by AOM ^c			20 798	17 802	12 519	11 206	8204	6284
Tp^*NiBr	in CH_2Cl_2	34 480 (3880)	29 410 (660)	20 080 (450)	17 420 (65,sh)	12 350 (140)	11 190 (138)		
	in CCl_4	31 500 (2400)	28 900 (640)	20 220 (630)	17 600 (90, sh)	12 320 (160)	11 110 (190)	absent ^b	6290 (60)
	by AOM ^c			20 232	17 593	12 325	11 072	8037	6326
Tp^*NiI	in CH_2Cl_2		27 930 (2880)	19 190 (700)	17 390 (120)	12 110 (150)	11 030 (123)		
	in CCl_4	27 250 (3120)	25 770 (3130)	19 300 (1140)	16 900 (190,sh)	11 980 (250)	10 890 (220)	absent ^b	6420 (70)
	by AOM ^c			19 295	16 902	11 979	10 904	7933	6408

^a Transitions from a ${}^3\text{A}_2({}^3\text{T}_1, \text{F})$ ground state. Splitting diagram shown in Figure S2. ^b Forbidden in C_{3v} symmetry. ^c The calculated band energies are those for the case of idealized C_{3v} symmetry and with $\epsilon_{\pi}(\text{N}) > 0$. Essentially identical values obtained for $\epsilon_{\pi}(\text{N}) \leq 0$. See Table 4 for parameters.

P_3NiX halides exhibited reversible nickel(II) to nickel(I) reductions, and the iodide offered the most thermodynamically accessible nickel(I) state, readily forming [(triphos)-Ni^I] in solution. In this Tp^*NiX series, the harder N_3 -donor ligand does not stabilize nickel(I) as well as the P_3 -donor; however, such a species could exist as an electronic excited state. The remaining bands are much weaker, are in the Vis–NIR region, and are common to all three Tp^*NiX complexes with a slight red shift from Cl to Br to I. This pattern of electronic absorption bands is characteristic of C_{3v} Tp^*NiX complexes.^{17,19} These Vis–NIR bands are thus assigned to electronic transitions which are primarily d–d in character. The strongest and highest energy of these appears near $20\,000 \text{ cm}^{-1}$; an additional weaker band is split into two components and appears near $12\,000 \text{ cm}^{-1}$, and a weak band is found in the NIR region near $6\,000 \text{ cm}^{-1}$. Band assignments in C_{3v} symmetry are summarized in Table 2. Ligand-field calculations, which exactly match (see Table 2) all of the observed transitions (Figure 2), place the ${}^3\text{A}_2({}^3\text{T}_1, \text{F}) \rightarrow {}^3\text{A}_1({}^3\text{T}_2, \text{F})$ symmetry-forbidden transition at $\sim 8000 \text{ cm}^{-1}$. Alternative band assignments, such as ${}^3\text{A}_2({}^3\text{T}_1, \text{F}) \rightarrow {}^3\text{A}_1({}^3\text{T}_2, \text{F})$ observed at $\sim 11\,000 \text{ cm}^{-1}$ along with the other bands correspondingly blue-shifted and ${}^3\text{A}_2({}^3\text{T}_1, \text{F}) \rightarrow {}^3\text{A}_2({}^3\text{A}_2, \text{F})$ either at $\sim 30\,000 \text{ cm}^{-1}$ or remaining at $\sim 20\,000 \text{ cm}^{-1}$ were rejected on the basis of AOM fits (poor matches to experimental transitions combined with unreasonable parameters). The slight distortions for Tp^*NiX that remove perfect 3-fold symmetry in the solid state are therefore relaxed or averaged out in fluid solution.

HFEPR of Tp^*NiCl . The HFEPR spectra of Tp^*NiCl recorded using optical modulation at any frequency higher than $\sim 250 \text{ GHz}$ consist of a group of three distinct features at low field (effective g of ~ 4.5 – 5 , depending on frequency), and a peculiarly shaped “flat tabletop” absorption centered around the $g \approx 2.3$ value (Figure 3, top). The use of standard field modulation results in a more conventional derivative-shaped EPR spectrum (Figure 3, bottom); however, the signal-to-noise ratio does not increase as the “tabletop” edges

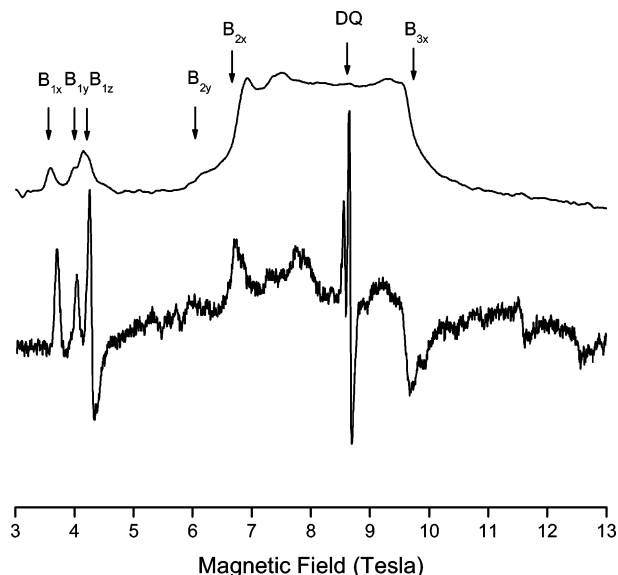


Figure 3. HFEPR spectrum of Tp^*NiCl at 276 GHz: (top) optical modulation of 250 Hz frequency with a temperature of 4.5 K and (bottom) magnetic field modulation of 40 kHz frequency and 2 mT amplitude with a temperature of 10 K. The particular turning points are labeled according to the standard triplet state practice.³⁰ DQ is the so-called “double-quantum” transition.

are quite broad. In addition some weaker but narrower features become much more pronounced in field-modulated spectra. These include the “double-quantum” transition at $g \approx 2.25$, which is dominant in the field-modulated spectrum,⁴¹ and some possible artifacts that show up throughout the field-modulated trace but are invisible in the optically modulated spectrum. The group of signals at $g_{\text{eff}} \approx 5$ shown in Figure 3 can be unequivocally identified as the $B_{1x,y,z}$ transitions (i.e., the three turning points corresponding to the nominally forbidden $\Delta M_S = \pm 2$ transitions for each of the three canonical orientations of the zfs tensor relative to the Zeeman

(41) The origin of this particular transition, which tends to appear in most Ni(II) systems is still being disputed, see: van Dam, P. J.; Klaassen, A. A. K.; Reijerse, E. J.; Hagen, W. R. *J. Magn. Reson.* **1998**, *130*, 140–144.

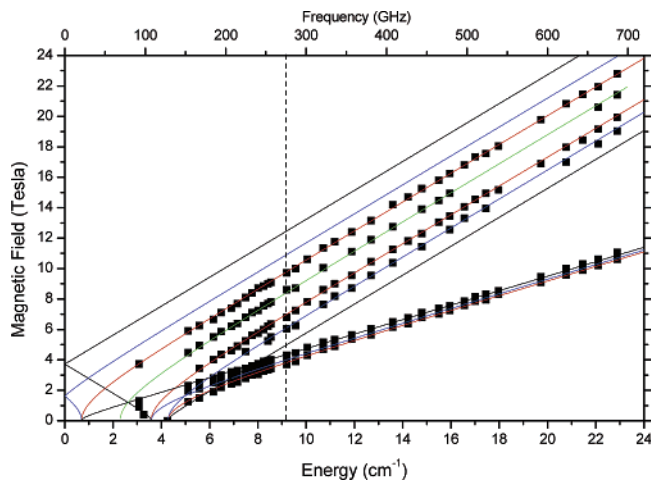


Figure 4. Resonance field vs frequency dependence of HFEPR resonances observed in Tp^*NiCl . The squares are experimental points, while the curves were generated using the best-fit spin Hamiltonian parameters, as in Table 3: (red lines) turning points with $B||x$, (blue lines) turning points with $B||y$, (black lines) turning points with $B||z$ (only the B_{1z} branch observed in experiment), and (green line) the double-quantum transition. The broken line at 276 GHz represents the frequency at which the spectra shown in Figure 3 were taken.

field). The tabletop feature requires more consideration. Its simplest interpretation requires an axial zfs tensor. The two edges of the pattern would then be the perpendicular turning points of the powder pattern corresponding to the $\Delta M_S = \pm 1$ transitions, and the distance between them (3 T) would correspond to D , which would thus be equal to $\sim 3 \text{ cm}^{-1}$. However, an attempt to simulate a spectrum at a given frequency shows that the $\Delta M_S = \pm 1$ features cannot be combined with the $\Delta M_S = \pm 2$ transitions using an axial zfs tensor. In addition, the very number of the $\Delta M_S = \pm 2$ transitions points at a rhombic zfs tensor. We have thus not tried to optimize spin Hamiltonian parameters from single-frequency spectra, but instead, we performed a multi-frequency experiment using tunable sources and collected the full 2D data set of resonance field versus frequency dependencies. This data set is presented in Figure 4 as squares.⁴² By fitting spin Hamiltonian parameters simultaneously to all the experimental points, we derived the most likely assignment of the observed resonances and thus the optimal parameters and errors associated with them. This assignment requires that the two edges of the tabletop absorption pattern correspond to the $B||x$ canonical orientation of the zfs tensor. The shoulder on the low-field side of this pattern corresponds to the $B||y$ canonical orientation, while its counterpart on the high-field side of the tabletop pattern is not visible. No parallel ($B||z$) turning points are observed in the spectra, which is not unusual, given that these features are usually the weakest in a powder pattern. The spin Hamiltonian parameters obtained through least-squares fits are collected in Table 3 and show that an optimized fit requires $|D| = 3.93 \text{ cm}^{-1}$ with a sizable value of $|E|$ equal to 0.35 cm^{-1} , which yields a rhombicity ratio ($|E/D|$) of about

(42) Although it is clear from Figure 4 that the frequencies higher than 400–450 GHz are redundant, we used the full available range of frequencies because we needed confirmation that no additional zero-field transitions appear at high frequencies.

Table 3. Experimental Spin Hamiltonian ($S = 1$) Parameters of the Tp^*NiX Series

complex	D (cm^{-1})	E (cm^{-1}) ^a	g_x	g_y	g_z
Tp^*NiCl	+3.93(2)	+0.348(9)	2.280(2)	2.265(6)	2.254(6)
Tp^*NiBr	-11.43(3)	-0.02(2)	2.232(5)	2.232 ^b	2.28(3)
Tp^*NiI	-23.01(4)	-0.74(4)	2.16 ^b	2.16 ^b	2.16(1)

^a The sign of E was assumed to be identical to that of D . ^b The g value was assumed (no experimental points available).

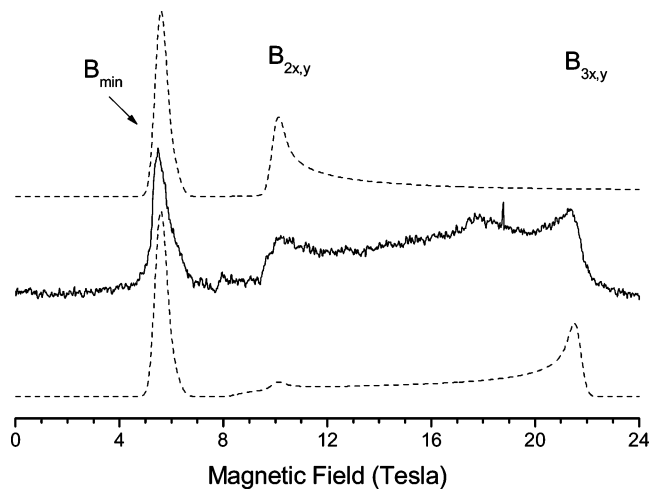


Figure 5. (middle) HFEPR spectrum of Tp^*NiBr optically modulated at 250 Hz, 527 GHz, and 4.2 K. (top) Simulation using $D = +13.43 \text{ cm}^{-1}$ ($E = 0$). (bottom) Simulation using $D = -13.43 \text{ cm}^{-1}$. The narrow line at 18.8 T is a DPPH marker, while the broad line near 17.6 T is the double-quantum transition.

10%. The data allow determination of all three canonical g values (Table 3), and the \mathbf{g} matrix is rhombic as expected from the sizable $|E/D|$. Since the single-frequency spectra could not be adequately simulated under the assumption of a perfect powder pattern, the sign of D could not be unequivocally established experimentally. However, the sign of D is positive in an analogous complex, $\text{Tp}^{\text{Bu}}\text{NiCl}$,⁴³ as well in the previously studied complex, $\text{Ni}(\text{PPh}_3)_2\text{Cl}_2$,¹ thus a positive D value can be assumed for Tp^*NiCl .

HFEPR of Tp^*NiBr . In contrast to those of Tp^*NiCl , single-frequency spectra of Tp^*NiBr could be convincingly reproduced by simulations assuming powder patterns. One such spectrum is shown in Figure 5, accompanied by simulations using both a positive and a negative value of D . It is clear that, in this case, D is negative. The accurate value of $|D|$ and the interpretation of the particular transitions were delivered by the resonance field versus energy dependence of the HFEPR spectra. Such a dependence for Tp^*NiBr , Figure 6, displays one prominent feature, which is a zero-field transition at about 350 GHz ($\sim 11.7 \text{ cm}^{-1}$). Upon variation of the frequency, this transition develops into at least three different branches, which were identified through simulations and are labeled in the caption to Figure 6. All spectral features are very broad, with line widths reaching 1 T. A fit of the frequency dependence of the observed resonances yields the set of spin Hamiltonian parameters given in Table 3. The zfs tensor is practically axial, with a

(43) Krzystek, J.; Ozarowski, A.; Trofimenko, S.; Telsler, J. Unpublished results.

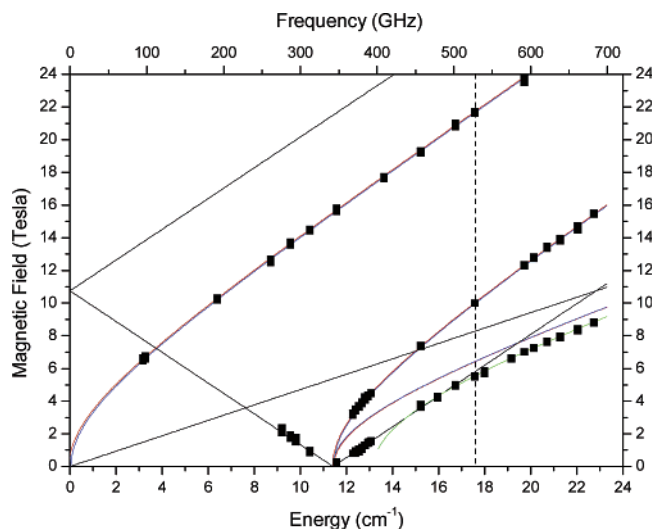


Figure 6. Resonance field vs frequency dependence of HF EPR resonances observed in Tp^*NiBr . The squares are experimental points while the curves were generated using the best-fitted spin Hamiltonian parameters as in Table 3: (red lines) turning points with $B_{||x}$, (blue lines) turning points with $B_{||y}$, (black lines) turning points with $B_{||z}$, and (green line) B_{min} . The broken line at 527 GHz represents the frequency at which the spectrum shown in Figure 5 was taken.

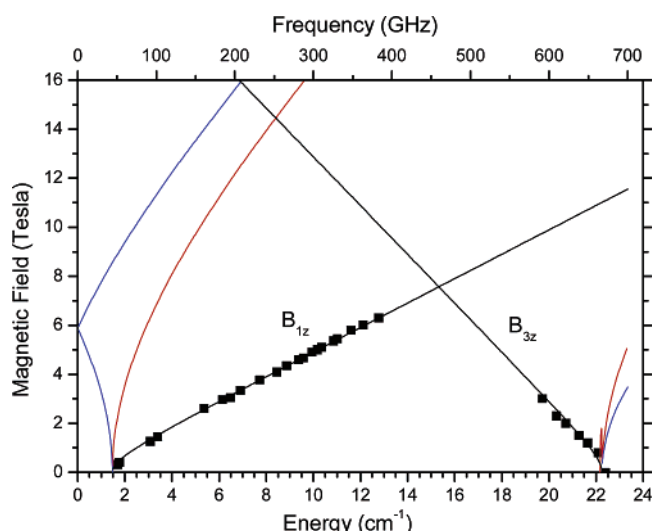


Figure 7. Resonance field vs frequency dependence of HF EPR resonances observed in Tp^*NiI at 4.5 K. The squares are experimental points, while the curves were generated using the best-fitted spin Hamiltonian parameters as in Table 3: (red lines) turning points with $B_{||x}$, (blue lines) turning points with $B_{||y}$, and (black lines) turning points with $B_{||z}$.

large $|D| = 11.43 \text{ cm}^{-1}$. In Tp^*NiBr , in contrast to the chloride complex, it is not possible to distinguish any rhombicity in the g values, which is as expected for this case of nearly axial zfs.

HF EPR of Tp^*NiI . Single-frequency spectra of Tp^*NiI are particularly poor in recognizable features, showing only one transition at any observation frequency. Rather than simulating such spectra, we proceeded to collect the resonance field versus frequency dependence of the observed transitions. The dominant feature of such a dependence in Tp^*NiI is the zero-field transition observed near 660 GHz (22 cm^{-1} , Figure 7). Because this frequency is at the very limit of our sources, we could follow only the high-field resonance branches originating from it into lower frequencies.

Another turning point is clearly visible at almost all frequencies employed below 400 GHz. The resonance field versus frequency dependence of this turning point (identified as B_{1z} through simulations) shows another zero-field resonance at about 45 GHz, and thus a finite value for $|E|$ of $\sim 0.75 \text{ cm}^{-1}$. The prominence of the B_{1z} feature and the absence of assignable perpendicular transitions at low frequencies, suggests that field-induced torquing of the crystallites prevents the observation of an ideal powder pattern. The least-squares fit of the spin Hamiltonian parameters to the observed resonances results in the values shown in Table 3. The zfs tensor is nearly axial with a very large $|D| = 23.01 \text{ cm}^{-1}$ and small $|E| = 0.74 \text{ cm}^{-1}$. The only other transition observable (at frequencies greater than 550 GHz) was assigned to the other parallel turning point, B_{3z} . Situations where the B_{1z} transition is observable in the 200–350 GHz frequency range, while the B_{3z} is not, are consistent with the $|+1\rangle$ and $|-1\rangle$ pair of levels lying lower in energy than the $|0\rangle$ level, which by convention corresponds to a negative value of D . Because the only resonances observable⁴⁴ belong to the parallel branches ($B_{||z}$), we were able to determine only the g_z value of 2.16. A nearly axial g tensor is expected in this complex, as in the bromide, thus we assume $g_x = g_y \approx g_z$ (Table 3).

AOM analysis of Tp^*NiX . The AOM analysis requires structural information on the metal ion coordination geometry. Structural information is available for the chloride²² and, now for the bromide complexes, providing necessary N–Ni–X bond angles and N–Ni–B–N torsional angles (yielding θ and ϕ , respectively; see Scheme 1). The bond and torsional angles used in the AOM analyses are tabulated in Table S3. The situation is complicated by the fact that the unit cells of both chloride and bromide complexes contain two structurally slightly different molecules. A further complication of the solid-state structures is that there are two relevant torsional angles that each yield the AOM parameter ϕ , and these differ slightly because of the nonplanarity of the pyrazole rings. For example, in Tp^*NiBr molecule 1, the torsional angle $\text{N}_1\text{–Ni}_1\text{–B}_1\text{–N}_4$ is 120.99° , while $\text{N}_3\text{–Ni}_1\text{–B}_1\text{–N}_2$ is 119.32° . The two relevant angles were thus averaged to yield ϕ values for AOM calculations. These torsion angles were incorporated into the AOM models using the formulation described by Schäffer.²⁴ The effect of nonplanarity was subsequently explored by including a small twist angle, $\psi \leq 1^\circ$, for the Tp^{*-} nitrogen ligands; however, this had little effect on the electronic energy levels.

In addition, although HF EPR studies were performed on microcrystalline solid samples, electronic absorption spectra were recorded in fluid solutions. AOM calculations for Tp^*NiX ($X = \text{Cl}, \text{Br}$) were therefore made on three different structural cases: molecules 1 and 2 in each unit cell, as described above, plus a putative C_{3v} complex in which the ϕ value was set to 120° (or 240°), and the θ value was made the weighted average of the four crystallographic X–Ni–N

(44) A “minority species” was present in the sample, generating resonances close to the $g \approx 2.2$ region at any frequency (not shown) that clearly cannot be brought in agreement with the dominant “majority species”.

angles. Such an idealized C_{3v} complex likely resembles the species found in CCl_4 or CH_2Cl_2 fluid solution.

For the iodide complex, perfect C_{3v} symmetry was likewise assumed, and a value of 124° was employed for all of the I–Ni–N angles, which is roughly equivalent to the Br–Ni–N average angle incremented by the difference between the average Cl–Ni–N and Br–Ni–N angles. The assumption of a similar structure for the iodide, comparable to the structurally characterized chloride and bromide, is based on the analogous series of zinc halides: $Tp^{tBu}ZnX$ ($X = Cl, Br, I$).³⁸ Down this series, the Zn–N bond length ranges from 2.045 (for Cl) to 2.073 Å (for I), and the X–Zn–N bond angle varies only from 120.3 – 121.3° .

In addition to structural information, AOM analysis requires bonding parameters (ϵ_σ and ϵ_π). We have previously estimated such parameters for halide ligands in the series $Ni(PPh_3)_2X_2$.¹ As in that study and elsewhere,^{45–47} we assume cylindrical π -bonding for the halides ($\epsilon_\pi x(s) \equiv \epsilon_\pi y(c)$) and employ our earlier values as starting points for ϵ_σ and ϵ_π values. Initial estimates of Tp^{*-} N-donor ligand parameters were taken from the work of Fujihara et al. that provided AOM parameters for $[(Tp)_2Cr]^+$,⁴⁸ noting that theirs is a six-coordinate chromium(III) ($3d^3$, $S = 3/2$) complex with unsubstituted pyrazoles ($Tp^- =$ hydrotris(pyrazolyl)borate, unmethylated form of Tp^{*-}). As in their case, we assume planar π -bonding for the Tp^{*-} ligands ($\epsilon_\pi x(s) \neq 0$, $\epsilon_\pi y(c) \equiv 0$).

With the above information as a starting point, AOM calculations effectively modeled the observed electronic transitions for Tp^*NiCl and enabled assignments of all spin-allowed transitions. These results are summarized in Table 2, and an associated splitting diagram of the triplet states of Tp^*NiCl is given as Figure S2. The quality of the AOM description of Tp^*NiX is indicated by the excellent agreement between the calculated spin-allowed transitions and the electronic spectra recorded over a wide range of energies. In the idealized cases, the calculated agreement with the experimental data in CCl_4 solution is exact. When the specific crystal structures are used, the lack of 3-fold symmetry means there are no 3E terms, and the fit can be to either one of resulting orbital singlets or to an average of the two. Consensus values for these fit models are given in Table 4. Nevertheless, calculated transitions, based on all the structural models, are within 5% of the experimental assignments. Concerning the uncertainties in the fit parameters, we found the value for B to be very robust; it varied by $< \pm 5 \text{ cm}^{-1}$ ($\sim 1\%$) regardless of model used. Uncertainties in the bonding parameters are difficult to determine because of the many assumptions involved, but the reported values can be considered to have a precision of roughly $\pm 100 \text{ cm}^{-1}$.

We found bonding parameters for the chloride that did not greatly differ from those for $Ni(PPh_3)_2Cl_2$. For the

bromide and iodide, bonding parameters larger than those previously reported (for $[Ni(PPh_3)X_3]^-$, $X = Br, I$,⁵¹ or for $Ni(L_N^+)Br_3$,⁴⁶ see Table 4) are required, although the ϵ_σ value does decrease in the order $Cl > Br > I$. These $[LNiX_3]$ complexes, however, are not ideal analogues because of the presence of three halo ligands, and we further suggest that the electronic absorption data in the Tp^*NiX series allows a more accurate determination of bonding parameters than was the case in those complexes. These larger bonding parameters in Tp^*NiX are consistent with significant covalent interactions between nickel and these halide ligands, as is also shown by the ligand contributions to the electronic spectra and the large magnitude zfs for bromide and iodide complexes (see below).

Successful fitting required a reduction in the value for nitrogen ϵ_σ ($\sim 6000 \text{ cm}^{-1}$ in all cases, see Table 4) compared to that given by Fujihara et al. (8350 cm^{-1}),⁴⁸ however, this is consistent with the weaker Lewis acidity of nickel(II) compared to chromium(III). For example, Δ_o for $[Cr(en)_3]^{3+}$ is 9000 cm^{-1} greater than that for the nickel(II) counterpart,⁴⁹ and a similar difference is observed for $[(Tp)_2Cr]^+$ versus $[Tp_2Ni]$ ($\Delta_o = 21\,790$ ⁴⁸ and $\sim 12\,000 \text{ cm}^{-1}$,⁵⁰ respectively); the ϵ_σ values for $[Cr(en)_3]^{3+}$ and $[Cr(NH_3)_6]^{3+}$ are $\sim 7200 \text{ cm}^{-1}$, while ϵ_σ for $[Ni(en)_3]^{2+}$ and $[Ni(NH_3)_6]^{2+}$ are 4000 and 3600 cm^{-1} , respectively.²³ The ratio of these parameters for Cr(III)/Ni(II) in these cases is ~ 1.8 versus ~ 1.4 here; however, the Tp^{*-} ligand is expected to be a stronger σ -donor than Tp^- , and these chromium(III) complexes also lack halide ligands, which are weaker σ -donors than the scorpionates.

The nature of π -bonding involving the pyrazole nitrogen ligands is not totally clear. Fujihara et al.⁴⁸ reported significant π -donation to Cr(III) and Co(III) ($\epsilon_\pi(N) = 1300 \text{ cm}^{-1}$), which was based not only electronic absorption spectroscopy but also on MCD and luminescence measurements that allowed observation of spin-forbidden transitions. With their values as a starting point, the fits of the electronic absorption bands for Tp^*NiX yielded $\epsilon_\pi(N) \approx 900 \text{ cm}^{-1}$. This π -bonding by Tp^{*-} is consistent with that found by Fujihara et al.⁴⁸ in that their ratio $\epsilon_\sigma/\epsilon_\pi = 6.4$ agrees closely with the range found here (6.2 – 7.1 , depending on the specific case, with the exception of Tp^*NiBr molecule 2).

Nevertheless, we explored the possibility of π -acceptor behavior by the pyrazole nitrogen ligands in the Tp^*NiX series with idealized geometries. The fits to the electronic absorption bands, with the same values for B , which resulted when the values for $\epsilon_\pi(N)$ were constrained negative were equally as good as those when positive values, initially based on those of Fujihara et al.,⁴⁸ were used. The resulting bonding parameters are quite different: for all X, $\epsilon_\sigma(X)$ and $\epsilon_\pi(X)$ are reduced by ~ 33 and $\sim 16\%$, respectively, and for $X = Br$ and I , $\epsilon_\sigma(N)$ is $\sim 15\%$ lower (unchanged for Cl). The values for $\epsilon_\pi(N)$, however, are negligibly small, essentially

(45) Gerloch, M.; Slade, R. C. In *Ligand-Field Parameters*; Cambridge University Press: Cambridge, U.K., 1973.

(46) Gerloch, M.; Manning, M. R. *Inorg. Chem.* **1981**, *20*, 1051–1056.

(47) Gerloch, M.; Hanton, L. R. *Inorg. Chem.* **1981**, *20*, 1046–1050.

(48) Fujihara, T.; Schönherr, T.; Kaizaki, S. *Inorg. Chim. Acta* **1996**, *249*, 135–141.

(49) Lever, A. B. P. *Inorganic Electronic Spectroscopy*, 2 ed.; Elsevier: Amsterdam, 1984.

(50) Jesson, J. P.; Trofimenko, S.; Eaton, D. R. *J. Am. Chem. Soc.* **1967**, *89*, 3148–3158.

(51) Hanton, L. R.; Raithby, P. R. *Acta Crystallogr.* **1980**, *B36*, 2417–2419.

Table 4. AOM-Derived Parameters and zfs Values (in cm^{-1}) Calculated from These Parameters for Tp^*NiX (this work) and Related Ni(II) Complexes^m

		B^a	ζ^a	$\epsilon_\sigma(\text{E})^b$	$\epsilon_\pi(\text{E})^c$	$\epsilon_\sigma(\text{X})$	$\epsilon_\pi(\text{X})^d$	calcd D^e	calcd $ E ^e$
$\text{Tp}^*\text{NiCl}^f,g$	idealized	580	347	6008	843	4832	1517	+3.93	0.00
	molecule 1	"	"	6100	900	4900	1400	+3.93	0.23
	molecule 2	"	"	5900	950	4500	1000	+3.89	0.35
	idealized with $\epsilon_\pi(\text{N}) \leq 0^h$	"	"	5904	-125	3304	1262	+3.93	0.00
Tp^*NiBr^f	idealized	563	635	6087	962	4591	1123	+11.24	0.00
	molecule 1	"	"	6050	910	4550	1095	+11.40	0.38
	molecule 2	"	"	5700	560	4000	1080	+11.37	1.20
	idealized with $\epsilon_\pi(\text{N}) \leq 0^h$	"	"	5164	-1	3091	939	+11.24	0.00
Tp^*NiI^f	idealized	498	1000	6082	976	4233	861	+22.48	0.00
	idealized with $\epsilon_\pi(\text{N}) < 0^h$	"	"	5130	-4	2719	724	+22.48	0.00
$\text{Ni}(\text{L}_\text{N}^+)\text{Cl}_3^i$		760	130	6100	0	3250	1000		
$\text{Ni}(\text{L}_\text{N}^+)\text{Br}_3^i$		720	120	5900	0	3000	850		
$[\text{Ni}(\text{PPh}_3)\text{Br}_3]^{-j}$		620	195	5000	-1500	3000	700		
$[\text{Ni}(\text{PPh}_3)\text{I}_3]^{-j}$		490	190	6000	-1500	2000	600		
$[\text{Ni}(\text{triphos})\text{I}]^{+k}$		- - -	440	855	-170	135	13.5		
$\text{Ni}(\text{PPh}_3)_2\text{Cl}_2^l$		480	435	5510	-1235	5230	2420	+13.2	1.8
		(460)	(345)	(4190)	-1675	(5690)	(1140)	(+12.6)	(3.6)
$\text{Ni}(\text{PPh}_3)_2\text{Br}_2^l$		590	264	4290	-500	3180	520	+7.1	1.4
$\text{Ni}(\text{PPh}_3)_2\text{I}_2^l$		480	550	5510	-1235	2000	600	+23.9	5.8

^a For comparison, the nickel(II) free-ion has values of $B = 1080 \text{ cm}^{-1}$ ($C/B \approx 4.7$) and $\zeta = 630 \text{ cm}^{-1}$.²³ See note *g* for discussion of the effect of variation in C . ^b $E = \text{N-}$ or P- donor ligand, as described below. ^c The specific nature of π -bonding is as defined for each N- or P-donor ligand. ^d Cylindrical π -bonding is assumed ($\epsilon_{\pi(\text{s})} \equiv \epsilon_{\pi(\text{c})}$) for the halide ligands in all cases. ^e Calculated from the splitting within the ground-state triplet; no sign determination of E is possible. ^f This work. The first set of values provides the best fit to the electronic absorption spectra in CCl_4 (see Table 2), assuming C_{3v} symmetry as likely found in solution. The following two sets of values each provides the best consensus fit to the electronic absorption spectra in CCl_4 , employing the crystal structure data for molecules 1 and 2 in the unit cell, respectively. For the N-donor ligands in Tp^* , the value only for $\epsilon_{\pi(\text{s})}$ is given: $\epsilon_{\pi(\text{c})} \equiv 0$, as in Fujihara et al.⁴⁸ These workers found $\epsilon_\sigma(\text{N}) = 8350$, $\epsilon_\pi(\text{N}) = 1300 \text{ cm}^{-1}$ for the N-donor ligands in $[\text{Tp}_2\text{Cr}]^+$, giving a ratio of $\epsilon_\sigma(\text{N})/\epsilon_\pi(\text{N}) = 6.4$. This ratio is in good agreement with the ratios given here for Tp^*NiX (6.2–7.1), with the exception of the Tp^*NiBr molecule 2. For Tp^*NiCl , calculations with an applied magnetic field were made for molecules 1 and 2, and the resulting Zeeman-split energy levels gave as an average of the two molecules $g_x = 2.2145(1)$, $g_y = 2.225(1)$, and $g_z = 2.1608(1)$, which can be compared to the experimental values in Table 3. No such calculations were performed for the other two Tp^*NiX complexes because of the discrepancy in sign of zfs. ^g All of the calculations listed employed $C/B \approx 4.7$, as in the free-ion.²³ However, for the case of idealized Tp^*NiCl with $\epsilon_\pi(\text{N}) > 0$, the effect of variation in C was explored. With all other parameters the same, $C/B \approx 4.3$ ($C = 2500 \text{ cm}^{-1}$) gave $D = +3.88 \text{ cm}^{-1}$ and $C/B \approx 4.9$ ($C = 2840 \text{ cm}^{-1}$) gave $D = +3.95 \text{ cm}^{-1}$. The adjustment of ζ from 347 to 349 or 346 cm^{-1} , respectively, restored $D = +3.93 \text{ cm}^{-1}$. ^h The possibility of π -acceptor properties of the Tp^* -pyrazole nitrogen atoms was explored by fits using the idealized geometries as described above but with $\epsilon_\pi(\text{N}) \leq 0$. Essentially identical fits obtained for the electronic absorption spectra and D values as for fits with $\epsilon_\pi(\text{N}) > 0$. ⁱ Reported by Gerloch and Manning;⁴⁶ values are based on magnetic measurements and electronic absorption spectroscopy. L_N^+ is *N*-ethyl-1,4-diazabicyclo[2.2.]octonium; $\epsilon_\pi \equiv 0$ for this tertiary amine donor ligand. ^j Reported by Gerloch and Hanton;⁴⁷ values are based on magnetic measurements and electronic absorption spectroscopy. Cylindrical π -bonding is assumed for PPh_3 in all cases. ^k Reported by Zanello et al.;⁴⁰ values are based primarily on electronic absorption spectroscopy. Triphos is $\text{CH}_3\text{C}(\text{CH}_2\text{PPh}_2)_3$; 1,1,1-tris(diphenylphosphinomethyl)ethane. These workers made the following ligand-field parameter assumptions: $Dq^1 = 350 \text{ cm}^{-1}$, where $Dq \equiv 3\epsilon_\sigma - 4\epsilon_\pi$, and $\epsilon_\pi(\text{I}) = (0.1)\epsilon_\sigma(\text{I})$, $\epsilon_\pi(\text{P}) = (-0.2)\epsilon_\sigma(\text{P})$ (cylindrical π -bonding for both I and P). These assumptions for iodine give the bonding parameters reported herein; their fits to the optical data then provided a value for $Dq^1 = 3250 \text{ cm}^{-1}$, which yields the value given here for $\epsilon_\sigma(\text{P})$. These workers also reported a value for spin-orbit coupling at $\sim 70\%$ of the free-ion value, which yields the value reported herein. No value for B was reported. ^l Reported by Krzystek et al.;¹ values (rounded here to the nearest 5 cm^{-1}) are based on magnetic measurements, HFEPR, and previously reported electronic absorption spectroscopy. Cylindrical π -bonding is assumed for the PPh_3 ligand in all cases. The set of values in parentheses for $\text{Ni}(\text{PPh}_3)_2\text{Cl}_2$ was determined with the constraint that $\epsilon_\pi(\text{Cl}) = (0.2)\epsilon_\sigma(\text{Cl})$. The values for $\epsilon_\sigma(\text{I})$ and $\epsilon_\pi(\text{I})$ in $\text{Ni}(\text{PPh}_3)_2\text{I}_2$ were chosen to equal those reported for $[\text{Ni}(\text{PPh}_3)_3]^{+}$.

zero for $\text{X} = \text{Br}$ and I and roughly -100 cm^{-1} for Cl , indicating minimal Ni–N π -interaction, which seems unlikely.

Given the good fit to the spin-allowed electronic absorption data, regardless of pyrazole π -bonding model, SOC was included to predict the zfs observed by HFEPR. For the chloride complex, the results were very satisfactory. The use of the same SOC constant in all three structural models (and in the idealized model with $\epsilon_\pi(\text{N}) \leq 0$) gave an exact match to the sign and magnitude of D , assuming that the sign of D in Tp^*NiCl is positive. The two crystal structure models also closely matched the observed rhombic splitting, E (see Tables 3 and 4). Note that the crystal structures do not require equivalence among all three N donors: only two are symmetry equivalent. Thus, if the unique N donor were allowed slightly different bonding parameters from the other two, then the calculated rhombic splitting could be increased.⁵² The value of ζ (347 cm^{-1}) for Ni(II) in Tp^*NiCl

is 55% of the free-ion value, and the value of the Racah parameter B is 54% of the free-ion value, indicating a consistent and reasonable reduction from free-ion values by the ligands in the chloride complex. The precision in ζ in this model is very high; variation by only $\pm 1 \text{ cm}^{-1}$ changes the calculated D value by 0.02 cm^{-1} , which is experimentally significant in HFEPR.

For the bromide and iodide complexes, the situation was quite different. It is possible to match the magnitude of the observed zfs only by use of unreasonably large values for ζ : the free-ion value for Tp^*NiBr and 160% of the free-ion value for the iodide. Equally problematic, the sign of D is calculated to be positive, as with the chloride, but it was experimentally found to be negative, as discussed above. Inclusion of the same value for ζ that was employed in the

(52) For example, in the idealized case for Tp^*NiCl , a shift in $\epsilon_\sigma(\text{N}3)$ by $+100 \text{ cm}^{-1}$ compensated by a shift for each of $\epsilon_\sigma(\text{N}1)$ by -50 cm^{-1} retained $D = +3.93 \text{ cm}^{-1}$ but generated $|E| = 0.10 \text{ cm}^{-1}$.

Nickel(II) Scorpionate Complexes

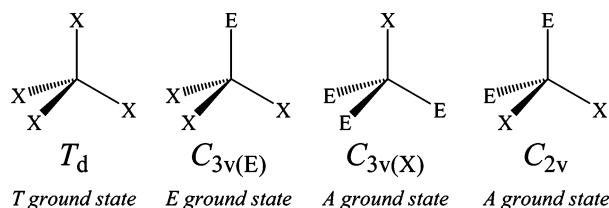


Figure 8. Related four-coordinate nickel coordination spheres in which halide ligands (X) are replaced with phosphorus or nitrogen donor ligands (E). The first and second C_{3v} geometries differ in whether a halogen or a nitrogen/phosphorus atom defines the C_3 axis, as indicated by the subscripts (X) or (E), respectively.

positive case gave the same calculated zfs (see Table 4). A d^8 ligand-field model is thus successful at describing zfs in the chloride complex but not in complexes with the heavier halides, Br and I.

Discussion

The present electronic and magnetic resonance spectroscopic measurements for Tp^*NiX complexes help to complete a series of related high-spin $C_{3v(X,E)}$ nickel(II) coordination spheres (Figure 8) including N_3X ,⁴⁶ PX_3 ,⁵¹ and P_3X donor sets.⁴⁰ These donor sets are compared in Table 4. Parameters $\epsilon_\sigma(P, I)$ and $\epsilon_\pi(P, I)$, which we extracted from the ligand field data of Zanello et al for $[(triphos)Ni]^{+40}$ are very different from those determined both here and by Gerloch,^{46,47} and a direct comparison of $[Ni(triphos)I]^{+}$ AOM parameters with others in the nickel(II) $C_{3v(X,E)}$ series does not appear productive at present.

In general, the AOM results indicate strong covalent σ - and π -bonding interactions between nickel(II) and the respective halide ligands. The strength of this interaction may impart thermodynamic stability to the Tp^*NiX complexes. Chloride has the largest σ -contribution of the three halides, and this correlates with the spectrochemical series. The ϵ_σ parameters determined for the nitrogen atoms of Tp^{*-} also indicate a very strong covalent interaction with nickel(II). Indeed, these ϵ_σ parameters are among the highest reported for nitrogen-donor atoms with pseudotetrahedral nickel(II), and these values approach the high ϵ_σ values seen for N-donors with cobalt(III) and chromium(III).²³ There is chemical precedent for strong covalent interaction of Tp^{*-} ligands with metal ions. One example compares the hydrolytic stability of $LiBH_4$ with Tm^*LiBH_4 .⁵³ Tm^* represents tris(3,5-dimethylpyrazolyl)methane, the neutral carbon-based analogue of Tp^{*-} . The ionic boron-hydride bonds of $LiBH_4$ are readily hydrolyzed by water. In Tm^*LiBH_4 , the Tm^* ligand imparts sufficient covalent character to the $[Tm^*Li]^{+}$ moiety, so that Tm^*LiBH_4 reacts much more slowly with ambient moisture.

Pyrazole, halogen, and nickel ionization potentials also support strong covalent interactions in Tp^*NiX . Gas-phase photoelectron spectroscopy (PES) of KTp^* indicated nitrogen lone-pair ionizations at 9.51 and 9.99 eV with π -ionizations ranging from 7.63 to 8.45 eV.⁵⁴ The first ionization energy for the halogens ranges from 10.44 eV for iodine to 12.97

for chlorine. Low-level DFT calculations for high-spin C_{3v} $TpMCH_3$ ($M = Fe, Co$) estimated the iron and cobalt partially filled d manifolds to fall in the range of 8.5–9.0 eV.¹⁹ A higher nuclear charge predicts that nickel d orbital ionization energies greater than 9 eV can be expected along with a greater covalent nickel–Tp interaction. Gas-phase UV PES measurements on $(Tp)_2M$ ($M = Fe, Co, Ni$) support this conclusion, where nickel d orbital ionizations (9.60 and 10.70 eV) were indeed higher than either cobalt or iron.⁵⁵ This correspondence in frontier orbital energy levels suggests that the effective σ - and π -overlap between nickel, pyrazole nitrogen atoms, and the halides, is energetically favorable and is particularly so for $[Tp^*Ni]^{+}$ with the lower-energy halogens, bromine and iodine. These points provide further support, albeit indirect, for the model of π -donation by the Tp^{*-} N ligands, as opposed to essentially no π -interaction, but we cannot be definitive at present. Experimental studies on a wider range of paramagnetic scorpionate complexes, in combination with computational studies, will help resolve the issue of M–Tp π -bonding.

The increase in Ni–X covalency upon going from Cl to Br to I is also reflected in the decrease in interelectronic repulsion, B , and by the increase in magnitude of zfs (see Table 4). Correspondingly, the $|D|$ value estimated for $Ni(Ph_3P)_2I_2$ was also large ($\sim 28 \text{ cm}^{-1}$).¹ The increased Ni–X covalency leads to a greater contribution of halide radical character to the electronic structure of the complex (Ni^I-X^{\bullet}). This LMCT species is the origin of the UV absorption band that red shifts and increases in intensity on going from Cl to Br to I. As discussed previously for the $Ni(Ph_3P)_2X_2$ series, this LMCT contribution increases $|D|$ because the SOC constant for Br and I atoms is much larger than for chlorine or that of the free nickel(II) ion.^{56–58}

The sign of D was not as fully addressed in the study on the $Ni(Ph_3P)_2X_2$ series ($X = Cl, Br, I$).¹ The positive sign of D was unequivocally determined to be positive for $Ni(Ph_3P)_2Cl_2$ and assumed to be positive for the other two halides. However, it is likely that for $Ni(Ph_3P)_2I_2$ (where D was determined only by powder magnetic susceptibility because no HFEP spectra were observable) the value of D is of large magnitude and negative, as is found here for Tp^*NiI . For $Ni(Ph_3P)_2Br_2$, there was likely maximum rhombicity ($|E| = |D|/3$) which greatly complicated determination of sign. Although direct comparison between the Tp^*NiX and $Ni(Ph_3P)_2X_2$ series is complicated by the difference in number of each ligand type and resulting symmetry, it

(53) Reger, D. L.; Collins, J. E.; Matthews, M. A.; Rheingold, A. L.; Liable-Sands, L. M.; Guzei, I. A. *Inorg. Chem.* **1997**, *36*, 6266–6269.

(54) Joshi, H. K.; Arvin, M. E.; Durivage, J. C.; Gruhn, N. E.; Carducci, M. D.; Westcott, B. L.; Lichtenberger, D. L.; Enemark, J. H. *Polyhedron* **2004**, *23*, 429–438.

(55) Bruno, G.; Centineo, G.; Ciliberto, E.; Bella, S. D.; Fragalà, I. *Inorg. Chem.* **1984**, *23*, 1832–1836.

(56) Moore, C. E. *Atomic Energy Levels*, circular 467; National Bureau of Standards: Washington, DC, 1958.

(57) Jørgensen, C. K. In *Absorption Spectra and Chemical Bonding in Complexes*; Pergamon Press: Oxford, U.K., 1962; p 159.

(58) The ζ values (in cm^{-1}) for Group 17 and 18 np^5 ($^2P_{3/2,1/2}$) atoms/ions derived from the energy levels given on the NIST/ASD web site (<http://physics.nist.gov/PhysRefData/ASD/index.html>), except for iodine,^{55,56} are as follows: $n = 2$ F 269.4, Ne^+ 520.2; $n = 3$ Cl 588.2, Ar^+ 954.4; $n = 4$ Br 2457, Kr^+ 3580; $n = 5$ I 5069 (ref 56, vol. III, p 106), Xe^+ 7025.

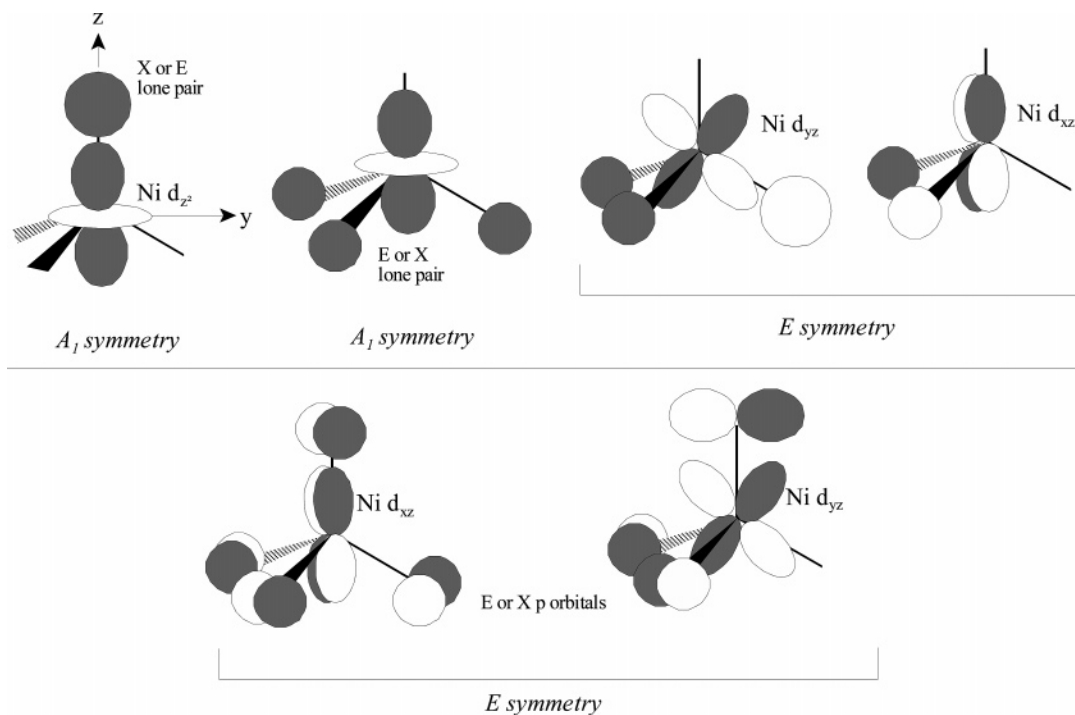


Figure 9. Depiction of σ -overlap (top) and π -overlap (bottom) involving nickel d orbitals and E/X derived symmetry adapted linear combinations within C_{3v} symmetry. The principal C_3 axis is along z , and the x axis is normal to the page (see upper left).

appears that a $3d^8$ ligand-field model with reasonable AOM bonding parameters describes well the electronic structure, including sign and magnitude of zfs, of Ni(II) with 2p and 3p ligand coordination (N, P, Cl). However, the sign and magnitude of zfs is not well described by this model for Ni(II) with 4p (Br) and, especially, 5p (I) ligand(s), despite the success of this model in describing the d–d electronic transitions in the entire Tp^*NiX series.

Significant spin–orbit contribution from bromine or iodine is capable of superseding the much smaller SOC from nickel, so that the halogen effect becomes the dominant spin–orbit contributor as was shown by Collingwood et al. in studies on the related complex $[NiI_4]^{2-}$.⁵⁹ In addition to being of large magnitude, it is possible for the halogen contribution to be of opposite sign to the nickel contribution, as was recently demonstrated for both T_d and distorted D_{2d} $[NiX_4]^{2-}$ geometries.⁶⁰ Also very important is the work by Mossin et al. on a six-coordinate manganese(III) ($3d^4$) complex, *trans*- $[Mn(\text{cyclam})I_2]I$ (cyclam = 1,4,8,11-tetraazacyclotetradecane).⁶¹ These workers showed quantitatively, using a valence-bond configuration interaction model, how the contribution to zfs from the iodide ligand(s) led to the D value for the complex being positive, rather than the negative value that is almost invariably observed for tetragonally distorted manganese(III).⁶¹ The present and previous^{59,60} work on nickel(II), manganese(III),⁶¹ and iron(III)⁶² show that an

unexpected sign of zfs is not an isolated phenomenon. Further theoretical investigation, not only in four-coordinate nickel(II) with iodo and bromo ligands but also with a variety of other metal ions and other np ($n > 3$) ligands, is thus needed.

Despite the present difficulty in fully characterizing the specific electronic structure of four-coordinate Ni(II) complexes with heavier donor atoms, several general conclusions about this class of complex are possible. The electronic ground state of C_{3v} nickel(II) complexes depends on the identity of the donor atom lying along the 3-fold axis of the complex. These possible structures, along with the parent tetrahedral and related C_{2v} complex, are shown schematically in Figure 8. When either nitrogen or phosphorus donors occupy this axial position (label $C_{3v(E)}$ in Figure 8), an orbitally doubly degenerate 3E electronic ground-state results, as has been reported by Gerloch and co-workers for both $Ni(L_N^+)X_3$ ($L_N^+ = N\text{-ethyl-1,4-diazabicyclo}[2.2.1]\text{octonium}$; a unidentate N-donor ligand; $X = Cl, Br$)⁴⁶ and $[Ni(PPh_3)X_3]^-$ ($X = Br, I$).⁴⁷ However, when a halogen occupies this axial site (label $C_{3v(X)}$ in Figure 8), an orbitally nondegenerate 3A_2 ground state results. This ground state is found not only for Tp^*NiX , but also for other $Tp^Y NiX$ complexes, where $Y = i\text{-Pr}, t\text{-Bu}, Me,$ or $p\text{-tolyl}$, and $X = \text{halide or pseudohalide}$.^{17,19} An 3A_2 ground state is therefore a general feature of nickel(II) $C_{3v(X)}$ complexes.

This difference in ground state between $C_{3v(X)}$ and $C_{3v(E)}$ nickel coordination spheres results from different levels of X/E σ -bonding with the d_z^2 , d_{xz} , and d_{yz} orbitals of nickel, as we describe here qualitatively. Nitrogen and phosphorus are predicted to be superior σ -donors compared to the halides, on the basis of the values for $\epsilon_\sigma(E) > \epsilon_\sigma(X)$. It is reasonable to assume that the d_z^2 , d_{xz} , and d_{yz} orbitals of nickel are best described as σ -antibonding for these complexes. The relevant

(59) Collingwood, J. C.; Day, P.; Denning, R. G. *J. Chem. Soc., Faraday Trans. 2* **1973**, 591–607.

(60) Atanasov, M.; Rauzy, C.; Baettig, P.; Daul, C. *Intl. J. Quantum Chem.* **2005**, *102*, 119–131.

(61) Mossin, S.; Weihe, H.; Barra, A.-L. *J. Am. Chem. Soc.* **2002**, *124*, 8764–8765.

(62) Zhang, Y.; Gebhard, M. S.; Solomon, E. I. *J. Am. Chem. Soc.* **1991**, *113*, 5162–5175.

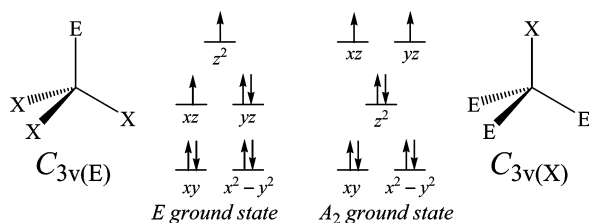


Figure 10. Nickel d orbital splitting diagrams in idealized C_{3v} symmetry that give rise to either a 3E electronic ground state, as in $Ni(L_N^+)Cl_3$, or a 3A_2 electronic ground state, as in Tp^*NiCl .

metal–ligand orbital interactions are shown in Figure 9. Given these considerations, the high-energy d_{z^2} orbital for $C_{3v(E)}$ likely results from dominant N/P σ -overlap of A_1 symmetry (i.e., along the $z \equiv C_3$ axis). The switch in d_{z^2} versus d_{xz} , d_{yz} ordering for $C_{3v(X)}$ results for two reasons. The d_{z^2} energy level drops because of the less dominant σ -bonding from X along z , while the d_{xz} , d_{yz} energy levels rise because these orbitals are strongly involved in σ -bonding with the three nitrogen atoms of $Tp^{* -}$. A qualitative d orbital splitting diagram for the $C_{3v(E)}$ and $C_{3v(X)}$ cases is shown in Figure 10. For simplicity, this diagram assumes idealized C_{3v} symmetry, which is valid particularly for Tp^*NiX in fluid solution.

Conclusions

Despite the relatively small steric bulk of the $Tp^{* -}$ ligand, it is possible to prepare stable four-coordinate complexes of the general formula Tp^*NiX for $X = Cl, Br, I$, from Tp^*NiBH_4 and the appropriate halocarbon. Strong Ni–X covalent bonding, as determined from a ligand-field analysis, accounts for the stability of the resulting complex. Tp^*NiX complexes have approximate C_{3v} point group symmetry and a spin triplet ground state ($S = 1$) with significant zero-field splitting, as high as $\sim 23\text{ cm}^{-1}$ for Tp^*NiI . Such systems are unsuitable for conventional EPR measurements, but HFEPN spectroscopy (frequencies up to $\sim 700\text{ GHz}$ with resonant fields up to 25 T) yielded spin Hamiltonian parameters for all three complexes. These results in combination with electronic absorption spectroscopy in the visible–NIR region have allowed ligand-field characterization of the electronic structure of Tp^*NiX . The model was fully

successful in characterizing Tp^*NiCl , but only partly so for the bromide and iodide complexes because of the large contribution to the zfs from the halide ligands. Previously reported four-coordinate nickel(II) complexes with C_{3v} point group symmetry, but with the general formula $[Ni(E)X_3]^{0-}$ ($E =$ unidentate, cationic N- or neutral P-donor ligand), have 3E electronic ground states. In contrast, the Tp^*NiX series (i.e., $[Ni(E)_3X]^{0-}$) exhibits a 3A_2 ground state. This difference results primarily from the strength of σ -bonding along the molecular z (C_3) axis, as shown by simple MO diagrams. The current results for Tp^*NiX can serve as a benchmark for the investigation of the electronic structure of nickel(II) in pseudotetrahedral geometry such as could be found naturally in biological nickel centers (e.g., nickel hydrogenase) and in nickel-substituted zinc and blue-copper proteins, where four-coordinate imidazole (histidine) ligation to metal(II) ions is common.

Acknowledgment. Financial support was provided by the donors of the American Chemical Society Petroleum Research Fund (39644-B3, P.J.D.), the University of Central Arkansas Research Council (P.J.D.), and by Roosevelt University (J.T.). HFEPN studies were supported by the National High Magnetic Field Laboratory, which is funded by the NSF through Cooperative Agreement DMR 0084173, the State of Florida, and the DOE. The 25 T resistive magnet was funded by the W. M. Keck Foundation. Funding from the Goldenberg Foundation supported purchase of a UV–vis–NIR spectrophotometer at Roosevelt University. We also thank Dr. J. Bendix, Ørsted Institute, Copenhagen, Denmark, for use of the program Ligfield and assistance with development of the program DDN.

Supporting Information Available: Complete listings of bond distances, angles, and atomic anisotropic thermal parameters for Tp^*NiBr , crystallographic data for this compound in CIF format, bond and torsional angles used in AOM analyses, figure showing UV–vis–NIR spectra of Tp^*NiX , a figure relating the triplet states for the T_d and C_{3v} systems. This material is available free of charge via the Internet at <http://pubs.acs.org>.

IC060843C